applied sciences

MDPI

Article

Thermal Behavior of Magnetic Scaffolds for RF-Induced Hyperthermia

Matteo Bruno Lodi [1,*], Raffaello Possidente [2], Andrea Melis [1], Armando Di Meglio [3], Alessandro Fanti [1] and Roberto Baccoli [2,*]

[1] Department of Electrical and Electronic Engineering, University of Cagliari, Via Marengo 2, 09123 Cagliari, Italy; andrea.melis89@unica.it (A.M.); alessandro.fanti@unica.it (A.F.)
[2] Department of Civil, Environmental and Architectural Engineering (DiCAAR), University of Cagliari, 09123 Cagliari, Italy; raffaello.possidente@unica.it
[3] Faculty of Technological and Innovation Sciences, University Mercatorum, Piazza E. Mattei, 00186 Roma, Italy; armando.dimeglio@unimercatorum.it
* Correspondence: matteob.lodi@unica.it (M.B.L.); rbaccoli@unica.it (R.B.)

Featured Application

This study supports the use of magnetic scaffolds with triply periodic minimal surface architecture as engineered agents for radiofrequency hyperthermia, highlighting their potential in targeted cancer treatment through improved thermal planning and predictable heat transfer behavior.

Abstract

Deep-seated tumors are challenging pathologies to treat. Currently available approaches are limited, prompting innovative solutions. Hyperthermia treatment (HT) is a thermal oncological therapy that raises tumor temperature (40–44 °C for 60 min), enhancing radio- and chemotherapy. Biomaterials loaded with magnetic particles, called magnetic scaffolds (MagSs), are used as HT agents for cancer treatment using radiofrequency (RF) heating. MagSs can be manufactured via 3D printing using fused deposition modeling to create biomimetic architectures based on triply periodic minimal surfaces (TPMSs). TPMS-based MagSs have been tested in vitro for RF HT. However, there is a lack of understanding regarding the thermal properties of TPMS MagSs for RF hyperthermia. Significant discrepancies between simulated and measured temperatures have been reported, attributed to limited knowledge of the apparent thermal conductivity of MagSs. Since planning is crucial for HT, it is fundamental to determine the thermal properties of these heterogeneous and porous composite biomaterials. Magnetic polylactic acid (PLA) scaffolds, shaped in different TPMS geometries and variable porosities, were thermally investigated in this research study. A linear relationship was found between the apparent thermal conductivity of parallelepiped and cylindrical scaffolds, and the measured values were validated using a numerical model of the RF HT test.

Keywords: 3D printing; heat transfer; hyperthermia; thermal properties; radiofrequency

Academic Editor: Ephraim Suhir

Received: 30 June 2025
Revised: 28 August 2025
Accepted: 3 September 2025
Published: 5 September 2025

Citation: Lodi, M.B.; Possidente, R.; Melis, A.; Di Meglio, A.; Fanti, A.; Baccoli, R. Thermal Behavior of Magnetic Scaffolds for RF-Induced Hyperthermia. *Appl. Sci.* **2025**, *15*, 9782. https://doi.org/10.3390/app15179782

1. Introduction

Deep-seated tumors, such as brain, cervical, and bone cancers, present significant challenges [1–3]. Current treatment options are limited, prompting the proposal of innovative solutions. One such approach is hyperthermia treatment (HT), a thermal oncological therapy aimed at raising the temperature of the tumor to 40–44 °C for 60 min, thereby

enhancing the effectiveness of radiotherapy and chemotherapy [4]. Hyperthermia uses heat as a drug, initiating a cascade of biological effects that ultimately help in battling cancers [5,6]. HT produces a cytotoxic environment, altering pH levels, inducing direct cell death, and impairing DNA repair mechanisms. Consequently, HT enhances the efficacy of radiotherapy and increases the permeability of tumor cells to chemotherapeutic drugs due to altered blood flow [5,6]. Therefore, combining HT with existing therapeutic modalities has been shown to manage advanced or inoperable cases more effectively, yielding higher rates of complete and durable responses compared to standalone treatments [5,6].

Various technologies are available to administer HT [7,8]. In other words, different forms of energy can be used to raise the temperature of tumors, exposing biological tissues to heat dissipation through various physical mechanisms [7]. The most commonly used methods are ultrasound (US) and electromagnetic (EM) energy [7]. Deep-seated tumors, which grow in challenging body sites at depths greater than 4–5 cm and in proximity to tissue interfaces (e.g., bone–muscle and fat–muscle) [9–11], present unique challenges. For these types of neoplasms, US HT has the drawback of difficult spatial and temporal temperature control due to significant reflections, particularly at the bone–soft tissue interface [7]. In a similar way, infrared radiation cannot be used at these depths, and it can be administered to the tumor only by means of catheters to perform local treatment, with the drawback of exposing the patient to infection risks [7]. On the other hand, due to the careful selection of working frequency and apparatus, EM-based HT technologies are often preferred in clinical practice for treating deep-seated tumors. Specifically, radiofrequency (RF) fields are used to expose patients to an electric field through capacitive electrodes or to induce RF currents using coils. Despite the advantages over US, research into RF HT for deep-seated tumors is still ongoing, with efforts focused on achieving optimal spatial temperature control while meeting clinical requirements [7,8,12]. The goal of RF HT is selective heating of tumor cells to avoid the overheating of non-target healthy tissues [7,8,12]. Consequently, more localized RF HT administration strategies have been proposed. In particular, the local heating of cancer has been thoroughly investigated in situ utilizing nanomaterials such as magnetic nanoparticles (MNPs) made of biocompatible iron oxides dispersed in a solution, administered to the tumor, and subsequently exposed to an RF magnetic field [13–15]. Magnetic fluid hyperthermia has been proposed as a tool against deep-seated tumors; however, the injection and delivery of significant magnetic nanoparticle (MNP) concentration to the tumor are challenging, limiting the applicability of this HT modality [7,13–15]. To address these shortcomings, the clinical management of deep-seated tumors, especially bone cancer [8,12], often requires surgical intervention and, sometimes, the implantation of a biomaterial graft to mechanically support healthy tissue and favor its repair [16].

In this context, biomaterials loaded with magnetic particles, known as magnetic scaffolds (MagSs), have been proposed as local interstitial hyperthermia agents for treating cancer using RF heating [17–22]. As reported in [17], several magnetic bioglass scaffolds have been reviewed. For instance, a 30CaO, 30SiO_2, and 40Fe_2O_3 (wt %) magnetic bioglass synthesized by melt quenching and having 100 emu/cm^3 saturation magnetization was tested with L929 cells to assess its biocompatibility [17]. Furthermore, 25CaO, (40 − x)SiO_2, 7P_2O_5, 3Na_2O, xZnO, and 25Fe_2O_3 glass–ceramics (x = 8, 10) were characterized using RF calorimetric techniques, and specific power losses of 20–30 W/kg were found. On the other hand, in [18], 3D-printed stents made of a polypropylene filament loaded with magnetite nanoparticles were characterized for the treatment of hollow organs, with the study finding power losses ranging from 60 W/g Fe at 95 kHz to approximately 250 W/g Fe at 270 kHz. These biomedical devices hold great potential in hyperthermia and deserve further studies.

MagSs can be manufactured according to chemical and physical routes, but recent studies have explored the use of 3D printing using fused deposition modeling (FDM) to achieve complex porous geometries and biomimetic architectures [18–22], which are necessary to meet mechanical, biological, and clinical requirements [17]. MagSs are designed and produced to be implanted in the tumor or following the surgical resection of a deep-seated tumor, such as bone cancer, as shown in Figure 1. After the placement of the MagSs, an RF magnetic field is applied using an induction heating coil or an electromagnet to trigger significant heat dissipation of the magnetic particles embedded in the biomaterial. This magnetothermal effect increases the temperature of the MagSs and facilitates the diffusion of heat into the surrounding (residual) tumor cells (Figure 1). Therefore, the temperature of the tumor can be increased to the therapeutic range of HT, resulting in increased effectiveness of chemotherapy and radiotherapy [18–22]. The temperature gradient from the MagSs to the tumor cells must be precise and controlled to avoid excessive heat diffusing to healthy cells. Following tumor control, the biomaterial implant can be exploited to allow for the healthy tissue to grow again and repair [19,20]. Despite the enormous clinical potential of MagSs, their design and modeling require further research efforts, especially from the perspective of thermal and electromagnetic engineering. Recently, it has been reported that the biomaterial porosity can impact the quality of HT [19]. It has been shown that the type of scaffold architecture and its porosity influence the heating and cooling rates, as well as the average scaffold temperature [19]. It has also been highlighted that the experimental determination of the specific absorption rate (SAR) in the target region requires specific protocols to cope with the porosity of 3D-printed MagSs [19,20]. In this framework, to accurately plan the HT of deep-seated tumors with MagSs, it is therefore essential to thoroughly investigate their thermal properties.

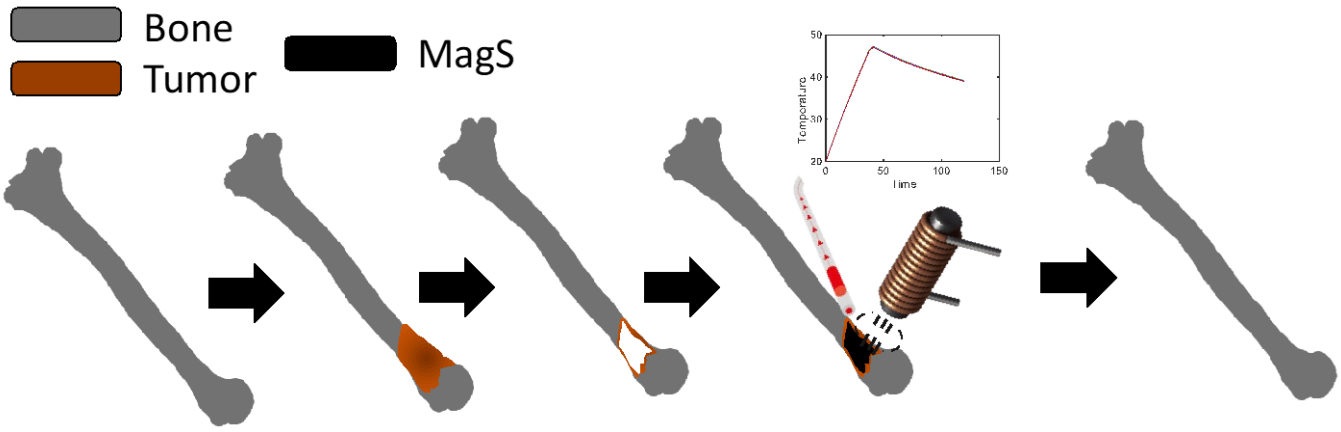

Figure 1. Use of magnetic scaffolds (MagSs) as hyperthermia agents against deep-seated tumors.

MagSs are porous nanocomposite materials. Therefore, discussion of the thermal properties of porous structures is necessary. Porous structures are often used in various thermal engineering applications, such as transpiration cooling in aerospace engineering and electronics, solar receivers, methane reformers, and catalytic converters [23]. Porous structures have been extensively studied for their potential in enhancing heat transfer. Zeigarnik et al. reviewed the use of porous materials for heat transfer [24,25]. The use of porous materials in heat exchangers is known to improve heat transfer by increasing the contact surface area [23–27]. These studies [23–27] collectively underscore the potential of porous structures in improving heat transfer efficiency.

Being a porous structure, MagSs' role in HT must be further elucidated. However, it must be recalled that the geometry and architecture (pore size, shape, and interconnectivity) of the biomaterial implants are supposed to be biomimetic while complying with

biomechanical requirements as well as mass transport properties, i.e., fluids and nutrient permeability [28,29]. In this framework, different methodologies for designing scaffold architecture have been proposed, such as unit cells based on different CAD-based primitives, space-filling curves, irregular structures, image-based methods, and implicit surface modeling [28,29]. Scaffold modeling using implicit surfaces is a flexible and effective approach that allows the description of implants with mathematical equations [29].

Among the different surfaces, a peculiar class has attracted researchers' attention. Triply periodic minimal surfaces (TPMSs) are popular implicit surfaces used as a basis to create solid porous implants with biomimetic features [19,30]. A TPMS is mathematically defined as a periodic surface with zero mean curvature [30,31]. Some classical TPMS structures include Schwarz primitive (P), Schwarz diamond (D), Schoen gyroid (G), Schoen I-graph (IG), and wrapped package-graph (IWP) structures [30,31], whose equations and unit cells are reported in Table 1. TPMS structures can be patterned in three mutually perpendicular directions to generate a lattice and can be additively manufactured [19,28–31]. TPMS solids are appealing for scaffold and tissue engineering applications due to their topological and mechanical properties. Their minimal surface nature ensures excellent mechanical properties, such as low stress concentration and high stiffness for orthopedic applications. Additionally, TPMS structures use less material while maintaining the strength used for scaffold manufacturing. Hence, porous TPMS structures present mechanical properties superior to conventional structures, making them efficient for scaffold manufacturing [19]. From the mass transfer perspective, TPMS structures offer several potential advantages over other porous structures, such as ease of functional grading, high specific surface area, enhanced pore connectivity, and biomimetic properties [19,28–31]. The possibility of using TPMS structure for heat transfer applications, however, has received little attention and has been poorly studied [32]. Notably, 3D-printable TPMS solids have been proposed as heat sinks [33]. It has been reported that the convective heat transfer performance of heat sinks depends on both the architecture's porosity and the architecture itself [34]. Since the surface area is higher than that of conventional structures, it has been hypothesized that TPMS structures could exhibit excellent heat transfer performance [33,34]. TPMS structures derived from the P surface are known to present an interstitial heat transfer coefficient higher than D and G surfaces [19]. G-surface heat exchangers have been reported to outperform those based on D and P surfaces [35].

Table 1. Equations and unit cell of triply periodic minimal surfaces (TPMSs).

TPMS Type	Equation ($\mathcal{F}$)	Unit Cell
Schwarz primitive (P)	$\cos(X)+\cos(Y)+\cos(Z)=K$	
Schwarz diamond (D)	$\cos(X)\cos(Y)\cos(Z)-\sin(X)\sin(Y)\sin(Z)=K$	
Schoen gyroid (G)	$\sin(X)\cos(Y)+\sin(Z)\cos(Z)+\sin(Y)\cos(Z)=K$	
Schoen I-wrapped package-graph (IWP)	$2[\cos(X)\cos(Y)+\cos(Y)\cos(Z)+\cos(X)\cos(Z)]-[\cos(2X)+\cos(2Y)+\cos(2Z)]=K$	
Lidinoid (L)	$\frac{1}{2}[\sin(2x)\cos(y)\sin(z)+\sin(2y)\cos(z)\sin(x)+\sin(2z)\cos(x)\sin(y)]-\frac{1}{2}[\cos(2x)\cos(2y)+\cos(2y)\cos(2z)+\cos(2z)\cos(2x)]+\frac{3}{20}$	

Despite these results, several general aspects of the heat transfer properties of TPMS structures must be elucidated. Furthermore, there is a need for investigating these properties to provide a reliable framework to empower the use of TPMS structures for thermal therapies in biomedical applications. Indeed, recently, MagSs based on TPMS and 3D printed using a magnetic polylactic acid (PLA) were tested in vitro for RF hyperthermia treatment of deep-seated tumors [19,20]. These biomedical devices exhibit intriguing therapeutic properties. However, there is a lack of understanding regarding the thermal properties of TPMS MagSs for RF hyperthermia. The thermal conductivity of the magnetic polymer was characterized following the ASTM F433 protocol using the Holometrix TCA 300 instrument (±3% precision) on 3D-printed, 100% dense samples with a cylindrical shape (diameter: 50.80 ± 0.25 mm, thickness: 2.29–12.7 mm, weight: 12.506 ± 0.13 g, density: 1.986 ± 0.04 g/cm^3) [36,37]. Compared to PLA, which has a thermal conductivity of $\lambda = 0.1849$ W/m·K, the magnetic PLA was found to have a thermal conductivity of 0.2943 W/m·K. Given that 3D printing via fused deposition modeling consist of the deposition of cylindrical fibers, the authors from [36,37] have hypothesized that air remains in the samples, even if they are printed with 100% infill density. Therefore, after correcting for a contribution of 13.75% volume fraction of air voids, the value of $\lambda = 0.4271$ W/m·K for the magnetic PLA was derived. Regarding specific heat, the ASTME1269-11 standard was used in [19], identifying a range of values for specific heat C_p between 1.10 and 1.2 J/gK. However, there is lack of knowledge regarding thermal conductivity and specific heat, thus calling for future studies.

However, using the thermal properties of magnetic PLA from [19,36], a significant discrepancy between the simulated and measured heating curves has been reported, attributed to the limited knowledge of MagS thermal conductivity and heat diffusivity. Since numerical planning is crucial in determining HT quality, it is essential to ascertain the thermal properties of heterogeneous and porous composite biomaterials. Therefore, this study characterizes TPMS magnetic polylactic acid (PLA) scaffolds considering different geometries and variable porosities. The derived apparent thermal conductivity was compared with the available literature data and validated using a numerical model of the RF HT test.

2. Materials and Methods

This section presents the materials, methodology, and experimental techniques used in this study. First, the mathematical formulation for the CAD modeling of the MagS TPMS architecture is discussed. Then, details about the magnetic PLA and the 3D printing process are provided. Subsequently, the experimental setup for determining the thermal properties of MagSs is described. The methodology for retrieving apparent thermal conductivity is discussed too. Finally, numerical simulations demonstrating the validity of the measured properties are presented.

2.1. TPMS Design

TPMSs are surfaces with mean zero curvature, belonging to the minimal surface class in $\mathbb{R}^3$ space. They exhibit a periodic behavior in the x, y, and z directions [19,31,38]. TPMSs can be mapped by Enneper–Weierstrass parametric representation using integrals in the complex domain, which is time-consuming from a computational perspective [19,31,38]. However, mapping TPMSs in Euclidean space using implicit functions reduces computational efforts. In Table 1, the most well-known functions that adapt to TPMSs are itemized. In this work, based on other literature works [23,28,31,33,35] and due to limited space, we will focus on gyroid and lidinoid geometries. Here, X, Y, Z, and K denote $\omega_x x$, $\omega_y y$, $\omega_z z$, and a constant value, with ω_i being the spatial periods (for $i = x, y, z$).

Different methodologies can be used to obtain a printable model from TPMS [19,38,39]. In this study, we used a Matlab interface previously developed and published by the authors in [32].

In brief, given a TPMS surface with law $\mathcal{F}$ from Table 1, the solid volume was generated by creating two offset surfaces ($\mathcal{F}_1(x,y,z) = K_1$, $\mathcal{F}_2(x,y,z) = K_2$, with $K_1 < K_2$), an inner and an outer one, that were linked and closed to form the final solid porous biomimetic architecture for the HT of deep-seated tumors. The surface junction, $\mathcal{F}_j$, was calculated considering the inequality $K_2 < \mathcal{F}_j < K_1$. Once the edge points of the surface were triangulated, the convex hull for the surfaces was determined. After removing the redundant, crossing, and non-manifold triangles, the connecting surfaces were determined, resulting in a closed domain. The model of the derived final solid was exported in stereolithography (STL) format (".stl") [38].

2.2. Magnetic PLA

TPMS MagSs were printed using the commercial magnetic-polymer composite filament Magnetic Iron PLA (Proto-Pasta, Vancouver, WA, USA), which consists of 10–40 wt.% of iron microparticles (~40 µm in size) [37]. The magnetic particle distribution in the fibers of these materials has been analyzed with scanning electron microscopy [19,20,36]. For the benefit of the readers, other details of the material are reported by the authors in [19,20].

2.3. 3D Printing

The printability of the geometry from the STL file was verified using Rhinoceros v7 (McNeel, Seattle, WA, USA) and IdeaMaker software (v 5.2.4, Shanghai, China). Finally, the scaffold samples were printed using the Raise3D Pro2 Plus 3D printer (Irvine, CA, USA) with the following settings: 0.45 mm nozzle, an extrusion temperature of 210 °C, a bed temperature of 45 °C, an infill density of 100%, and a printing speed fixed at 50 mm/s.

We 3D-printed a set of gyroid scaffolds with dimensions of 3 cm × 3 cm × 8 cm. The gyroid geometry was selected for its appealing heat transfer features based on references [23,28,31,33,35]. The porosity θ_p of the scaffolds varied from 0% to 85%. We selected gyroid because this topology is known to outperform Schwarz-P surface conjugate thermal transport [40]. We tested an additional set of three 3D-printed cylindrical scaffolds with a diameter of 8 cm and a height of 4 cm. We printed a non-porous reference sample and two different scaffolds made from a gyroid and a lidinoid surface [31,38,39]. The cylindrical MagSs are reported in Figure 2, and their weights and porosities are given in Table 2.

Table 2. Details of 3D-printed magnetic scaffolds.

Parallelepiped Magnetic Scaffolds		
Porosity (%)	**Weight (g)**	**Type**
0%	128	-
30%	97	Gyroid (G)
50%	69	Gyroid (G)
70%	40	Gyroid (G)
85%	21	Gyroid (G)
Cylindrical Magnetic Scaffolds		
0%	333	-
64%	121	Lidinoid (L)
85%	50	Gyroid (G)

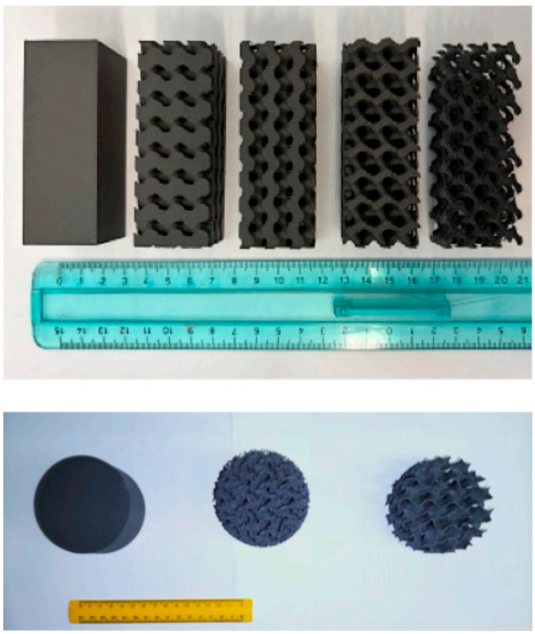

Figure 2. Image of 3D-printed magnetic scaffolds used in this study.

2.4. Measurements Setup

In this work, we utilized a validated experimental setup developed by the authors in [41] with the aim of determining the thermal conductivity (λ) of solid materials [41–43]. Interested readers are invited to refer to that paper for further details about mathematical and technical aspects. The measurement prototype, which housed a solid sample to be characterized, is shown in Figure 3. The apparatus was composed of three main modules: (i) a module with two Peltier cells able to supply a thermal power up to 100 W, (ii) two control boards coupled with the heat source, and (iii) a LabView (v2022Q3, Austin, TX, USA) application. The heating sources operated both as sources and sinks, subjecting the specimen to a controlled time-variable temperature gradient. The specimen was equipped with a guard ring made of certified material having a high thermal resistivity equal to ρ = 29.4 mK/W and a thickness of 8 cm. The working surface area of the Peltier cells was $S = 0.230 \cdot 0.122$ m^2. In addition, 10 mm thick aluminum plates were integrated into the heating modules, each equipped with four PT-1000 thermoresistance sensors (DIN Class, maximum error of 0.08 °C at 0 °C).

The temperature sensor values were used as feedback signals to adjust the thermal power according to the selected temperatures on the cold and hot sides. To measure the ambient temperature, an additional PT1000 thermistor was placed outside the device. Two custom heat flux meters (HFMs) with sensitivity equal to 4.14 and 4.04 W/m^2·mV were deployed in contact with the Peltier cells, overlapping their working active surfaces thoroughly, to measure the heat fluxes (HFs) across them [41]. The electrical signals sourced by the HFMs were acquired at 75 samples per second, with a resolution of 0.02 °C and an upper limit heat flux value equal to 331.2 W/m^2. Considering that the used apparatus works under the approximating assumption of a semi-infinite solid whose boundary is subject to a constant heat power equal to a maximum heat flux, such a limit value can be derived from the thermal diffusivity time product coefficient inequality, as explained in [41]. Supplementary T-type thermocouples were arranged inside the HFMs with the aim of acquiring the absolute and differential surface temperatures of the specimen. Two thermocouples were connected in differential fashion to reduce the error of the temperature difference. The sample under test was sandwiched between the two HFMs and tightened by a calibrated clamping screw system to ensure good and repeatable thermal contact [41].

An auxiliary thermocouple was added to the measurement system and placed in contact with the sample at a known position. The thermocouple was calibrated using melting ice, as shown in Figure 3a,b. The MagS samples were placed in a cavity within a polystyrene block (Figure 3c). The thermal conductivity of the polystyrene, considered as a reference material with known properties, was also assessed to further validate the measurement methodology. For the measurements on the seven MagS samples, a temperature gradient of ± 10 °C relative to the initial ambient temperature was applied across the specimen faces. This temperature gradient was selected to account for the upper limit for heat flux measurements [41]. Measurements continued until heat losses became minimal and the steady state for the heat fluxes (HFs) was fully established. The recorded temperature and HF signals were then used to determine the thermal properties of the MagSs.

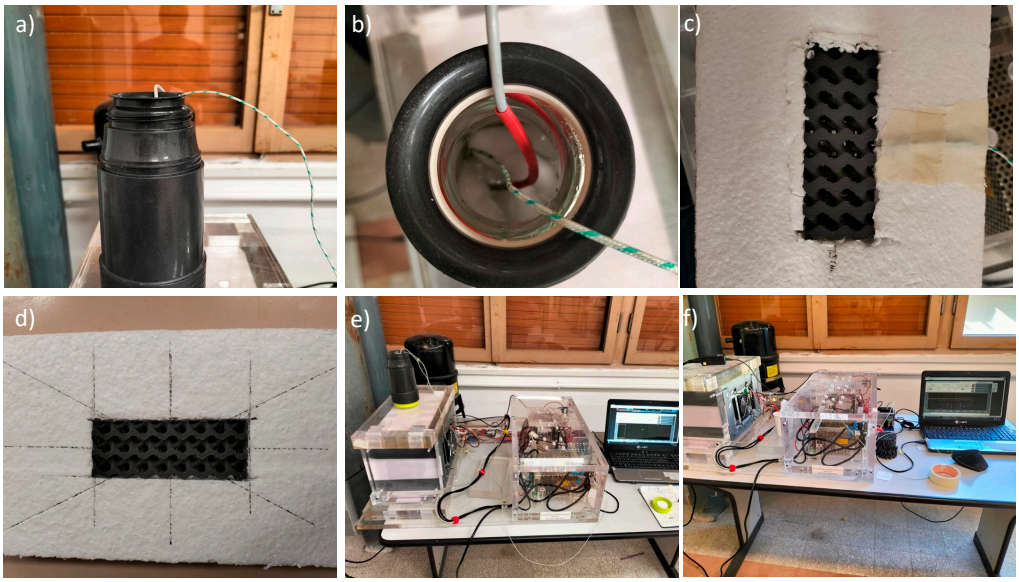

Figure 3. Experimental setup. (**a**) Calibration procedure for the thermocouple. (**b**) Details of the probe placement. (**c**) Sample within the polystyrene frame. (**d**) Geometrical details of the sample. (**e**,**f**) Photos of the experimental setup.

2.5. Thermal Characterization and Estimation of Apparent Thermal Conductivity

The original experimental device and the optimization technique for determining the effective thermal conductivity (λ) of solid materials from [41] were used in this work. We considered a macroscopic approach and treated the system considering the operating conditions, thus accounting for all other aspects in the measured λ, such as any possible convective motion and radiative exchanges that may occur due to the variable MagS porosity. The inverse problem of the classical steady-state Fourier heat equation was addressed numerically using an optimization procedure to determine boundary conditions based on measurements. Readers can refer to [41] for further details. Imperfect adiabatic behavior on the insulated lateral surfaces was accounted for by introducing heat loss correction functions through additional time-dependent Robin boundary conditions [41].

2.6. Numerical Simulations and Validation

We aimed to use the measured apparent thermal conductivity to validate the experimental finding of the calorimetric characterization of MagSs reported in [19,20]. Our findings will help refine the modeling of these functional biomaterials, thereby paving the way for more effective treatment planning with these innovative devices.

The finite element method (FEM) solver COMSOL Multiphysics v5.5 (COMSOL Inc., Burlington, MA, USA) was used to develop a numerical equivalent of the experimental

setup from [19,20] for specific absorption rate (SAR) measurements performed on a homogeneous cylindrical scaffold made with Proto-Pasta magnetic PLA. In brief, the scaffold was placed in an agarose cylinder (height 2.5 cm, diameter 2 cm, 10 mg·mL^{-1} [19,20]), to suppress convective phenomena, as shown in Figure 4. Indeed, water phantoms cannot be used due to the insurgence of convective heat transfer due to the relevant water volume and temperature gradient in this type of experiment [19]. In [19,20], optical probes were used to measure the temperature. Four points were selected. A probe was placed in the scaffold center. Then, two probes were placed 5 mm away from the edges of the scaffolds, one on the right (labeled as East) and one on the left (labeled as West) border. Finally, a probe was placed in the agar phantom, 5 mm away from the scaffold top surface. For the sake of clarity, the sampling points are presented in Figure 4. The three different samples S1F, S2F, and S4F from [19,20] were considered, corresponding to three different porosities, ranging from 6% to 64%. In particular, S2F has a 64% porosity, whilst S4F has a 20% porosity, and S1F corresponds to 6%.

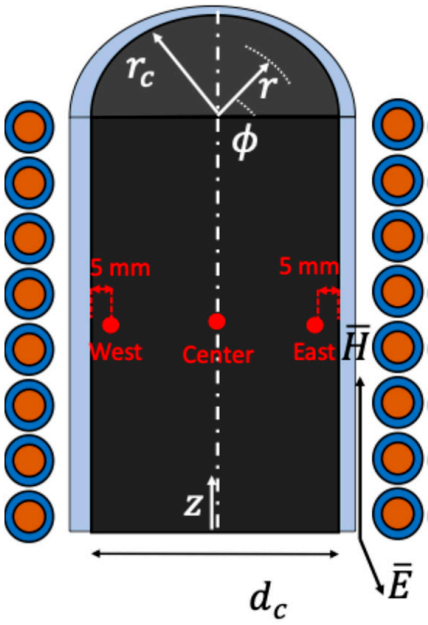

Figure 4. Schematic system geometry for the numerical simulations, with reference to the temperature sampling points.

Specifically, to use the experimentally derived thermal properties of MagSs to explain the calorimetric RF measurements from [19,20] for system geometry (Figure 4), we solved the frequency domain formulation of Maxwell's equations using the AC/DC module assuming a quasi-static process. The solution of these equations using the vector potential formulation allowed us to compute the magnetic flux density field vector ($\boldsymbol{B}$) of 30 mT produced by the 8-turn copper coil (coil diameter d_c = 2.54 cm, height h_c = 4.3 cm, coil wire diameter d_{sc} = 0.53 cm) inside the sample and the background agar media. The scaffold was modeled as a homogeneous cylinder with height h_c and diameter d_c, as shown in Figure 4. The induction heating coil was modeled as a homogenized multi-turn coil. The power dissipated by the magnetic scaffolds (P_m) was evaluated as $P_m = fA_{hyst}$, where f = 365 kHz is the working frequency (in hertz) and A_{hyst} is the area of the hysteresis loop derived from the static magnetic measurements (in joules), scaled by the specific density of the magnetic polymer sample [19,20]. The dielectric losses in the polymer and surrounding medium were computed as $P_e = \frac{1}{2}\sigma\left|\boldsymbol{E}^2\right|$, with $\boldsymbol{E}$ being the electric field vector (in volts per meter) and σ the electrical conductivity (in siemens per meter). Both the local and time-varying magnetic fields were considered. To solve the RF problem, the magnetic

vector potential was assumed to be zero at the initial time $\forall\, r, z$, whilst magnetic insulation was imposed at the boundaries of the air domain surrounding the coil, agar, and scaffold.

The total RF power ($P_{EM} = P_m + P_e$) dissipated by the ferromagnetic scaffold is the source term of a heat transfer equation. Such an RF heating problem is ruled by the steady Fourier's equation, from which the temperature pattern and dynamics in the specimen can be determined. For the selected FEM software, the Heat Transfer in Solid module was adopted. The steady-state assumption is justified by the uncertainties associated with the specific heat of the ferromagnetic polymer [19,20], which demand further investigations. Therefore, given that the experiments in [19,20] were performed considering a relatively long exposure, the term $\frac{\partial T}{\partial t} \to 0$. In mathematical terms,

$$\nabla \cdot (\lambda \nabla T) + P_{EM} = 0 \tag{1}$$

where λ is the thermal conductivity (W/m·K). The samples' physical properties were derived from the measurements. Therefore, in simulations, the cylinder was homogeneous but with an apparent thermal conductivity equal to a porous one. The agar thermal properties were taken from [19,20]. The initial temperature was assumed to be homogeneous in the system (T_0 = 19 °C $\forall\, r, z$) [19]. As a boundary condition for the thermal problem, convective heat flux was assumed at the top, bottom, and lateral surfaces. From the measurement setup described in [19,20], considering the time to reach the steady state and given that the induction coil was water-cooled, a value of equivalent surface heat transfer coefficient $h_c = 30$ W/m^2·K was assumed.

3. Results

We used the apparatus described in Section 2.5 and the methodology described in Section 2.6 to derive the effective thermal conductivities of the samples prepared with the geometries and porosities described in Section 2.3. The heat fluxes and temperatures, as well as the apparent thermal conductivity for all measurements, are available in the Supplementary Materials. The findings on the apparent thermal conductivity derived for the MagS sample (see Figure 2) are presented in Figure 5 and Table 2. It can be observed that, for both the parallelepiped and cylindrical scaffolds, the apparent thermal conductivity exhibits a linear decrease as porosity increases. The thermal conductivity value obtained in the absence of pores represents the thermal conductivity of the materials that make up the MagS samples (0.08 W/m·K—see Figure 5). It is observed that the apparent thermal conductivity of the sample decreases as the percentage of porosity increases, as reported in Table 2, since the air trapped in the pores acts as a thermal insulator when at rest. This trend is reversed when the porosity reaches a sufficient level (70%) to onset convective heat transfer mechanisms caused by air movement (see Table 2). This is confirmed by the TPMS-based MagSs with 85% porosity, since an increase of about 1.3% is observed (Table 3, Figure 5). The change in the linear decrease in the effective thermal conductivity with the increase in porosity ranges between 70% and 85% porosity values, thus showing that as porosity increases, there exists a point after which the heat transfer modifies due to the onset of convection. The experimentally observed mild increase in the effective thermal conductivity allows us to deduce that a non-fully developed convective heat flux mechanism is present. This behavior highlights how porosity can be positively exploited to enhance the heat transfer mechanism by convection using a pore-filling fluid with a higher density than air. For materials with a porous structure, the overall thermal conductivity is generally like that of a structure with uniformly distributed pores of the predominant size [19]. To better understand this point, we explored the asymptotic behavior of the limiting case of 100% porosity, which corresponds to the measurement of the effective thermal conductivity when the polystyrene sample holder is empty and an air cavity

($3 \times 3 \times 8$ cm^3) is present in the measurement apparatus (see Supplementary Materials). From Figure 5, it can be noticed that an effective thermal conductivity of ~0.075 W/m·K is derived, i.e., ~3 times the value of the thermal conductivity of dry air (i.e., ~0.025 W/m·K). This is due to the insurgence of convective phenomena. To numerically confirm such experimental results, we applied the correlation recommended in [44] for the natural convection heat transfer mechanism across enclosures, where two parallel finite surfaces were kept isothermal at temperatures T_1 and T_2 and spaced a distance apart with height L, and the top and bottom of the enclosure were insulated.

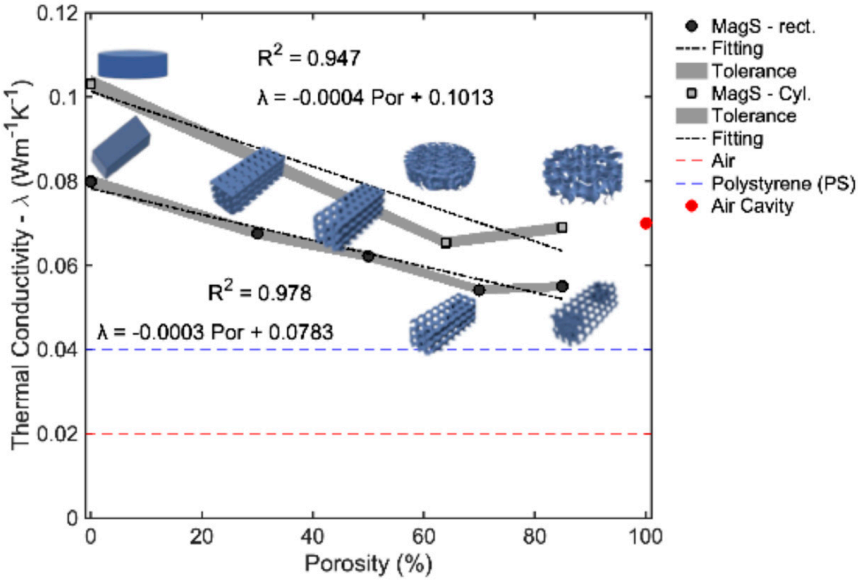

Figure 5. Measured effective thermal conductivity (λ, in Wm^{-1}K^{-1}) as a function of the sample porosity.

Table 3. Thermal conductivity of parallelepiped 3D-printed magnetic scaffolds.

Porosity (%)	Thermal Conductivity (λ, W/m·K)
0%	0.07984 ± 0.0015968
30%	0.06759 ± 0.0013518
50%	0.0622 ± 0.001244
70%	0.0542 ± 0.001081
85%	0.0549 ± 0.001980

For this geometry a special Nusselt number can be defined by the following relationship:

$$Nu = \frac{\lambda_{e,a}}{\lambda_{a,0}} = 0.071 \cdot \left(\frac{L}{b}\right)^{-\frac{1}{9}} \cdot (GrPr)^{1/3}$$

where $\lambda_{e,a}$ is the enhanced and effective thermal conductivity due to the convective effects in the enclosed space, $\lambda_{a,0}$ is the reference value of the thermal conductivity of air in equilibrium, L is the distance between the height of the enclosure, b is the distance between the faces of the enclosure, and Gr and Pr are the Grashof and Prandtl numbers [44], respectively. For the applied temperature gradient, with air viscosity of ~0.019 [mPa·s], $L = b = 3$ [cm], and $Pr = 0.7$, the derived $Gr = 3.96428 \cdot 10^5$, which corresponds to $Nu = 3.586$. In other words, $Nu \cdot \lambda_{a,0} = \lambda_{e,a}$. Considering the fact that natural convection can occur in the air cavity, we also used a hot wire anemometer (Terman, LSI, IT) to measure the air velocity in the enclosed space at the geometrical center of

the enclosure and recorded velocity values that gravitate around values close to 1 cm/s. Therefore, we further corroborated the validity of our measurements. Furthermore, as can be observed from Figure 5, we did not consider this point in the linear regression for the trend of the effective thermal conductivity as a function of the porosity, since these experiments were meant to provide insight into the heat transfer characteristics of our measurements.

For the cylindrical samples, a quasi-linear variation ($R^2 = 0.94$) of the apparent thermal conductivity of the ferromagnetic porous polymers as a function of the porosity is observed (see Figure 5 and Table 4). Remarkably, depending on the type of geometry and pore topology (i.e., gyroid or lidinoid), the apparent λ decreases differently as porosity increases. By comparing the cylindrical case with the rectangular-shaped case, it can be seen that a ~26% difference exists for all cases. This can be mechanistically explained considering that, for similar porosity values, lidinoid structures have a lower surface area and weaker thermal performance than their gyroid counterparts [23,28,31,33,35].

Table 4. Thermal conductivity of cylindrical 3D-printed magnetic scaffolds.

Porosity (%)	Thermal Conductivity (λ, W/m·K)
0%	0.10314 ± 0.00206
64%	0.06542 ± 0.00131
85%	0.0690 ± 0.00138

Considering the findings from Figure 5 and Tables 2 and 3, to further corroborate their validity, the measured apparent thermal conductivity values were used as input to simulate the RF calorimetric measurements on porous magnetic scaffolds from [19,20] for samples with 6, 20, and 64% porosities. The findings are reported in Figure 6. As shown in Figure 6a, for the magnetic flux density distribution, where the field is clearly more concentrated in the cylindrical magnetic material, the power dissipation takes place via hysteresis losses in the 3D-printed scaffold volume depending on the local field values, whilst in the surrounding agarose phantom, induced RF currents act as a volumetric source. The associated heat flux pattern is shown in Figure 6b. The steady-state temperature distribution for a 64% magnetic scaffold is shown in Figure 6c. Relatively high temperature gradients can be noticed in Figure 6c, reaching 37.5 °C/cm. In [19,20], optical probes were used to measure the temperature in the scaffold center, in the right and left edges 5 mm away from the center, at center height, and in the agar phantom 5 mm from the scaffold top surface (Figure 4). Therefore, from the multiphysics simulations performed using the measured effective thermal conductivity values, the temperature values for the three tested samples were extracted at similar test points and compared to the values reported in [19,20]. The findings are reported in Figure 6d–f. For the 64% porous scaffold, the average relative percentage error is ~−9%, showing that the simulated values are underestimating actual measured temperatures (Figure 6d). A clarification is therefore necessary. Even though in this case, the sample is the more porous one, i.e., the one with less mass, and the dissipated power per unit volume is supposed to be the lowest one, during the experiments from [19,20], the recorded temperatures are the highest. Given that the placement of the optical fibers is non-trivial, the recorded temperatures may have been performed at the material surface rather than in the pore space [19,20]. Therefore, the apparently high relative percentage error is not concerning. Furthermore, by comparing with the simulated results from [19,20], which made use of an estimated thermal conductivity value of about 0.47 W/mK (i.e., ~5–10 times higher than our measured values), it is possible to notice an average 33% error on the predicted peak temperature values. On the other hand, for the cylinder

with 20% porosity and gyroid geometry, the simulated temperature values are very close to the measured ones, reaching a very small error in all three points, as clearly visible in Figure 6e. For the less porous sample (6%), with a lidinoid architecture, the simulations resulted in a slightly lower temperature value, similar to our findings and the literature [23,28,31,33,35], with a ~−2% relative percentage error in the lateral points and reaching a 0.34% error in the cylinder center. By comparing the findings from Figure 6 to the simulated results from [19,20], the temperature values obtained using the measured apparent thermal conductivity are clearly closer to the experimental ones. Indeed, a noticeable increase in the predictive power is found. In [19,20] the simulation errors range from a minimum of ~3 °C to a maximum of 20 °C. Therefore, with our new numerical results, we have also verified the validity of the thermal characterization while fostering the clinical translation of 3D-printed TPMS-based MagSs for RF hyperthermia treatment of deep-seated tumors.

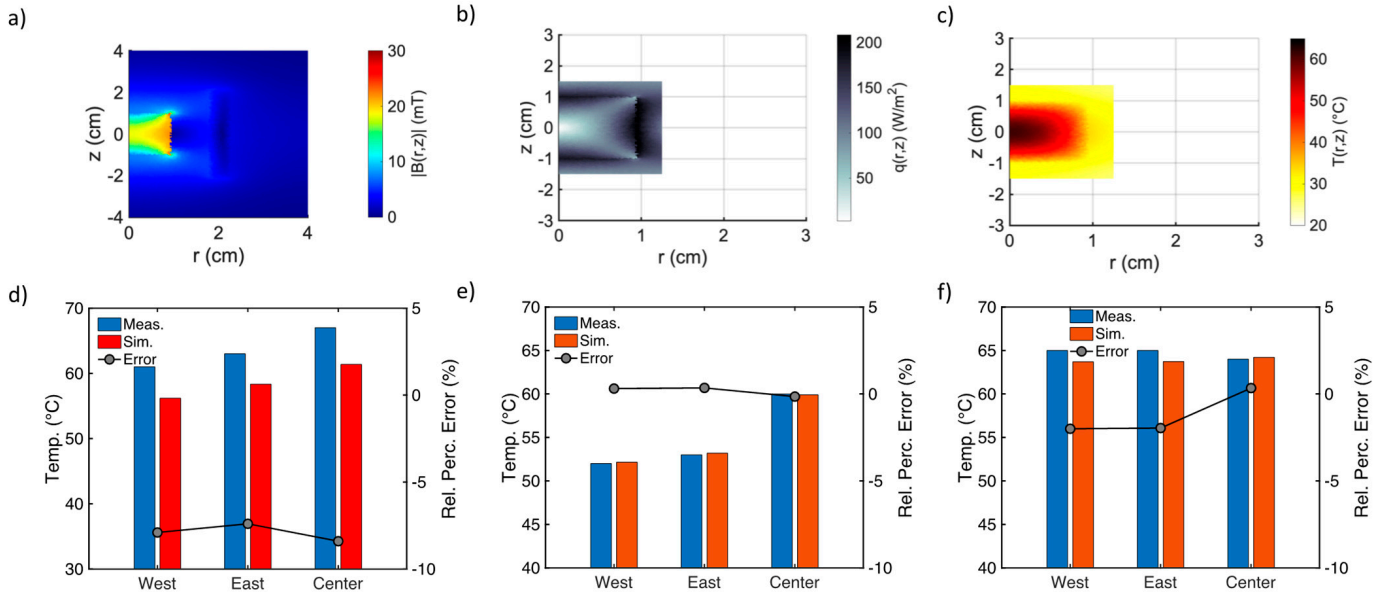

Figure 6. (**a**) Magnetic density flux distribution (in tesla). (**b**) Heat flux (in W/m^2). (**c**) Temperature pattern (in °C). Measured and simulated temperature and relative percentage errors for magnetic scaffolds with (**d**) 64%, (**e**) 20%, and (**f**) 6% porosities.

4. Conclusions

TPMSs are topologies that offer unique opportunities for customizing porous media and enhancing the performance of thermal management systems [29]. However, there is a lack of understanding and multiphysics modeling for leveraging recent advances in FDM and the transition from passive selection to active design of porous media in specific applications, i.e., customizing printable porous structures with designed pore features, such as porosity, pore size, and pore density. Among the applications for which TPMS can be appealing is the realm of biomedical applications, especially prosthetics and cancer therapy. In particular, after surgical resection of deep-seated tumors, magnetic scaffolds with TPMS architecture can be used as thermo-seeds when exposed to radiofrequency magnetic fields and increase the temperature of residual cancer cells. Moreover, 3D-printable TPMS-based MagSs can be easily manufactured, covering patient-specific geometry, and their scale-up and regulatory approval follow the magnetic fluid hyperthermia pathway [15]. However, despite these promising features, the thermal properties, especially the thermal conductivity, of these biomedical devices have been poorly studied. This study focused on characterizing the thermal conductivity of TPMS magnetic polylactic acid (PLA) scaffolds

with various geometries and porosities, in particular, primitive surfaces embedded in parallelepiped and cylindrical shapes and porosities ranging from 0% to 70%. To meet this aim, a specific methodology to estimate the apparent thermal conductivity was proposed, and an in-house apparatus was used. The obtained apparent thermal conductivity values were compared with existing literature data and validated using a numerical model of the RF HT test.

Future Directions

The next step could be to evaluate the thermal behavior of different TPMS topologies (e.g., D, P, and IWP surfaces) while accounting for the impact of surface roughness and irregularities or when the pores are filled with fluids denser than air, e.g., water or agar. Furthermore, the proposed methodology could be used to investigate how TPMS geometry in different shapes will behave from a thermal point of view. Advanced numerical analysis aimed at elucidating the pore-scale flow field may be carried out to elucidate the microscopic behavior of the relevant heat transfer quantities. Also, microscopic observation data (e.g., particle image velocimetry, PIV) could be analyzed and compared to simulations. Another relevant point to be investigated in future studies is the behavior of 3D-printed TPMS MagSs in vitro. So far, the magnetic polymer characterized in this study has been tested with BEAS2B, MRC-5, Huh-7, and a549 cell lines, showing increased metabolic activity compared to non-magnetic scaffolds [45]. Cytotoxicity experiments at 40–44 °C will be conducted to verify its effectiveness against tumoral cells while keeping healthy tumor cells safe. Therefore, future works will be focused on complementing the RF, thermal, and biological characterization of TPMS MagSs, thus allowing for the translation of these innovative biomedical devices in clinical practice as tools for fighting different tumors, such as bone cancer.

Supplementary Materials: The following supporting information can be downloaded at https://www.mdpi.com/article/10.3390/app15179782/s1.

Author Contributions: Conceptualization, R.B. and M.B.L.; methodology, R.B. and M.B.L.; software, all authors; validation, R.B., A.D.M. and M.B.L.; formal analysis, all authors; investigation, all authors; resources, R.B. and A.F.; data curation, M.B.L., A.M. and R.P.; writing—original draft preparation, M.B.L. and R.B.; writing—review and editing, all authors; visualization, R.P., A.M. and M.B.L.; supervision, R.B. and A.F.; funding acquisition, A.F. and R.B. All authors have read and agreed to the published version of the manuscript.

Funding: The research leading to these results received funding from the European Union—NextGenerationEU through the Italian Ministry of University and Research under PNRR—M4C2-I1.3 Project PE_00000019 "HEALITALIA" to Matteo Bruno Lodi and Alessandro Fanti, CUP F53C22000750006, University of Cagliari. The funding agency did not play any role in the conceptualization, design, or execution of the research. This work was supported in part by the Italian Ministry of Enterprises and Made in Italy (MIMIT), within the "ACCORDI PER L'INNOVAZIONE" (2021–2026), through the Project AISAC—Tecnologie ICT e dell'Industria 4.0 per l'Analisi e l'Ingegnerizzazione di Sistemi Alimentari Complessi per la produzione di pani artigianali locali ad alto valore aggiunto under Grant CUP: B29J23001120005.

Institutional Review Board Statement: Not applicable.

Informed Consent Statement: Not applicable.

Data Availability Statement: The raw data supporting the conclusions of this article will be made available by the authors on request.

Conflicts of Interest: The authors declare no conflict of interest.

Disclaimer Statement: The views and opinions expressed are those of the authors only and do not necessarily reflect those of the European Union or the European Commission. Neither the European Union nor the European Commission can be held responsible for them.

Abbreviations

The following abbreviations are used in this manuscript:

FDM	Fused Deposition Modeling
HF	Heat Flux
HFM	Heat Flux Meter
HT	Hyperthermia Treatment
MagSs	Magnetic Scaffolds
PLA	Polylactic Acid
RF	Radiofrequency
STL	Stereolithography
TPMS	Triply Periodic Minimal Surfaces

References

1. Zhu, S.; Lin, S.; Han, R. Treating Deep-Seated Tumors with Radiodynamic Therapy: Progress and Perspectives. *Pharmaceutics* **2024**, *16*, 1135. [CrossRef]
2. Nakahara, S.; Ohguri, T.; Kakinouchi, S.; Itamura, H.; Morisaki, T.; Tani, S.; Yahara, K.; Fujimoto, N. Intensity-Modulated Radiotherapy with Regional Hyperthermia for High-Risk Localized Prostate Carcinoma. *Cancers* **2022**, *14*, 400. [CrossRef]
3. Duke University. Innovative Antibody Approach Targets Deep-Seated Cancer Mutations. Available online: https://medicalxpress.com/news/2023-10-antibody-approach-deep-seated-cancer-mutations.html (accessed on 20 January 2025).
4. Bonferoni, M.C.; Rassu, G.; Gavini, E.; Sorrenti, M.; Catenacci, L.; Torre, M.L.; Perteghella, S.; Ansaloni, L.; Maestri, M.; Giunchedi, P. Electrochemotherapy of Deep-Seated Tumors: State of Art and Perspectives as Possible "EPR Effect Enhancer" to Improve Cancer Nanomedicine Efficacy. *Cancers* **2021**, *13*, 4437. [CrossRef]
5. Feldmann, H.J.; Seegenschmiedt, M.H.; Molls, M. Hyperthermia—Its Actual Role in Radiation Oncology. Part III: Clinical Rationale and Results in Deep-Seated Tumors. *Strahlenther. Onkol.* **1995**, *171*, 251–264.
6. Oei, A.L.; Kok, H.P.; Oei, S.B.; Horsman, M.R.; Stalpers, L.J.A.; Franken, N.A.P.; Crezee, J. Molecular and Biological Rationale of Hyperthermia as Radio- and Chemosensitizer. *Adv. Drug Deliv. Rev.* **2020**, *163*, 84–97. [CrossRef] [PubMed]
7. Kok, H.P.; Cressman, E.N.K.; Ceelen, W.; Brace, C.L.; Ivkov, R.; Grüll, H.; ter Haar, G.; Wust, P.; Crezee, J. Heating Technology for Malignant Tumors: A Review. *Int. J. Hyperth.* **2020**, *37*, 711–741. [CrossRef] [PubMed]
8. Paulides, M.M.; Dobsicek Trefna, H.; Curto, S.; Rodrigues, D.B. Recent Technological Advancements in Radiofrequency- and Microwave-Mediated Hyperthermia for Enhancing Drug Delivery. *Adv. Drug Deliv. Rev.* **2020**, *163*, 3–18. [CrossRef]
9. Gassie, K.; Alvarado-Estrada, K.; Bechtle, P.; Chaichana, K.L. Surgical Management of Deep-Seated Metastatic Brain Tumors Using Minimally Invasive Approaches. *J. Neurol. Surg. A Cent. Eur. Neurosurg.* **2019**, *80*, 198–204. [CrossRef]
10. Tuzzato, G.; Laranga, R.; Ostetto, F.; Bubbico, E.; Vara, G.; Bianchi, G. Primary High-Grade Myxoid Liposarcoma of the Extremities: Prognostic Factors and Metastatic Pattern. *Cancers* **2022**, *14*, 2657. [CrossRef] [PubMed]
11. Lee, S.Y.; Fiorentini, G.; Szasz, A.M.; Szigeti, G.; Szasz, A.; Minnaar, C.A. Quo Vadis Oncological Hyperthermia (2020)? *Front. Oncol.* **2020**, *10*, 1690. [CrossRef]
12. Kakehi, M.; Ueda, K.; Mukojima, T.; Hiraoka, M.; Seto, O.; Akanuma, A.; Nakatsugawa, S. Multi-Institutional Clinical Studies on Hyperthermia Combined with Radiotherapy or Chemotherapy in Advanced Cancer of Deep-Seated Organs. *Int. J. Hyperth.* **1990**, *6*, 719–740. [CrossRef]
13. Dutz, S.; Hergt, R. Magnetic Particle Hyperthermia—A Promising Tumour Therapy? *Nanotechnology* **2014**, *25*, 452001. [CrossRef]
14. Attaluri, A.; Kandala, S.K.; Zhou, H.; Wabler, M.; DeWeese, T.L.; Ivkov, R. Magnetic Nanoparticle Hyperthermia for Treating Locally Advanced Unresectable and Borderline Resectable Pancreatic Cancers: The Role of Tumor Size and Eddy-Current Heating. *Int. J. Hyperth.* **2020**, *37*, 108–119. [CrossRef] [PubMed]
15. Rubia-Rodríguez, I.; Santana-Otero, A.; Spassov, S.; Tombácz, E.; Johansson, C.; De La Presa, P.; Teran, F.J.; Morales, M.d.P.; Veintemillas-Verdaguer, S.; Thanh, N.T.K.; et al. Whither Magnetic Hyperthermia? A Tentative Roadmap. *Materials* **2021**, *14*, 706. [CrossRef] [PubMed]
16. Dakhale, R.; Paul, P.; Achanta, A.; Ahuja, K.P.; Meshram, M. Nanotechnology Innovations Transforming Oral Health Care and Dentistry: A Review. *Cureus* **2023**, *15*, e46423. [CrossRef]

17. Danewalia, S.S.; Singh, K. Bioactive Glasses and Glass-Ceramics for Hyperthermia Treatment of Cancer: State-of-Art, Challenges, and Future Perspectives. *Mater. Today Bio* **2021**, *10*, 100100. [CrossRef] [PubMed]
18. Mues, B.; Bauer, B.; Roeth, A.A.; Ortega, J.; Buhl, E.M.; Radon, P.; Wiekhorst, F.; Gries, T.; Schmitz-Rode, T.; Slabu, I. Nanomagnetic Actuation of Hybrid Stents for Hyperthermia Treatment of Hollow Organ Tumors. *Nanomaterials* **2021**, *11*, 618. [CrossRef]
19. Lodi, M.B.; Makridis, A.; Carboni, N.M.; Kazeli, K.; Curreli, N.; Samaras, T.; Angelakeris, M.; Mazzarella, G.; Fanti, A. Design and Characterization of Magnetic Scaffolds for Bone Tumor Hyperthermia. *IEEE Access* **2022**, *10*, 19768–19779. [CrossRef]
20. Lodi, M.B.; Makridis, A.; Kazeli, K.; Samaras, T.; Angelakeris, M.; Mazzarella, G.; Fanti, A. On the Evaluation of the Hyperthermic Efficiency of Magnetic Scaffolds. *IEEE Open J. Eng. Med. Biol.* **2023**, *5*, 88–98. [CrossRef]
21. Ortolani, A.; Bianchi, M.; Mosca, M.; Caravelli, S.; Fuiano, M.; Marcacci, M.; Russo, A. The Prospective Opportunities Offered by Magnetic Scaffolds for Bone Tissue Engineering: A Review. *Joints* **2016**, *4*, 228–235. [CrossRef]
22. Makridis, A.; Kazeli, K.; Kyriazopoulos, P.; Maniotis, N.; Samaras, T.; Angelakeris, M. An Accurate Standardization Protocol for Heating Efficiency Determination of 3D Printed Magnetic Bone Scaffolds. *J. Phys. D Appl. Phys.* **2022**, *55*, 435002. [CrossRef]
23. Cheng, Z.; Xu, R.; Jiang, P.X. Morphology, Flow and Heat Transfer in Triply Periodic Minimal Surface Based Porous Structures. *Int. J. Heat Mass Transf.* **2021**, *170*, 120902. [CrossRef]
24. Zeigarnik, Y.A.; Polyaev, V.M. Heat Transfer in Porous Structures: State of the Art and Main Lines of Study. *Therm. Eng.* **1996**, *43*, 70–79.
25. Zeigarnik, Y.A.; Ivanov, F.P. Choice of Efficient Linear Scale and Generalized Description of Internal Heat Transfer Coefficient in Porous Structures. *J. Eng. Thermophys.* **2018**, *27*, 36–44. [CrossRef]
26. Delavar, M.A.; Azimi, M. Using Porous Material for Heat Transfer Enhancement in Heat Exchangers. *J. Eng. Sci. Technol. Rev.* **2013**, *6*, 14–16. [CrossRef]
27. Ali, H.M.; Janjua, M.M.; Sajjad, U.; Yan, W.M. A Critical Review on Heat Transfer Augmentation of Phase Change Materials Embedded with Porous Materials/Foams. *Int. J. Heat Mass Transf.* **2019**, *135*, 649–673. [CrossRef]
28. Oladapo, B.I.; Kayode, J.F.; Karagiannidis, P.; Naveed, N.; Mehrabi, H.; Ogundipe, K.O. Polymeric Composites of Cubic-Octahedron and Gyroid Lattice for Biomimetic Dental Implants. *Mater. Chem. Phys.* **2022**, *289*, 126454. [CrossRef]
29. Giannitelli, S.M.; Accoto, D.; Trombetta, M.; Rainer, A. Current Trends in the Design of Scaffolds for Computer-Aided Tissue Engineering. *Acta Biomater.* **2014**, *10*, 580–594. [CrossRef]
30. Han, L.; Che, S. An Overview of Materials with Triply Periodic Minimal Surfaces and Related Geometry: From Biological Structures to Self-Assembled Systems. *Adv. Mater.* **2018**, *30*, 1705708. [CrossRef]
31. Jones, A.; Leary, M.; Bateman, S.; Easton, M. Parametric Design and Evaluation of TPMS-like Cellular Solids. *Mater. Des.* **2022**, *221*, 110908. [CrossRef]
32. Qureshi, Z.A.; O'Neill, W.; Thomas, D. Thermal Characterization of 3D-Printed Lattices Based on Triply Periodic Minimal Surfaces Embedded with Organic Phase Change Material. *Case Stud. Therm. Eng.* **2021**, *27*, 101315. [CrossRef]
33. Al-Ketan, O.; Ali, M.; Khalil, M.; Rowshan, R.; Khan, K.A.; Abu Al-Rub, R.K. Forced Convection CFD Analysis of Architected and 3D Printable Heat Sinks Based on Triply Periodic Minimal Surfaces. *J. Therm. Sci. Eng. Appl.* **2020**, *13*, 021010. [CrossRef]
34. Al-Ketan, O.; Rowshan, R.; Al-Rub, R.K.A. Topology-Mechanical Property Relationship of 3D Printed Strut, Skeletal, and Sheet Based Periodic Metallic Cellular Materials. *Addit. Manuf.* **2018**, *19*, 167–183. [CrossRef]
35. Li, W.; Li, W.; Yu, Z. Heat Transfer Enhancement of Water-Cooled Triply Periodic Minimal Surface Heat Exchangers. *Appl. Therm. Eng.* **2022**, *217*, 119198. [CrossRef]
36. Laureto, J.; Tomasi, J.; King, J.A.; Pearce, J.M. Thermal Properties of 3-D Printed Polylactic Acid-Metal Composites. *Prog. Addit. Manuf.* **2017**, *2*, 57–71. [CrossRef]
37. ProtoPasta. Iron PLA. Available online: https://proto-pasta.com/products/magnetic-iron-pla?srsltid=AfmBOooMUp5L6q2vWoKtWcFH0xr8h6mp7ZYcpio8XvzzfP-PJc293mMj (accessed on 27 August 2025).
38. Al-Ketan, O.; Abu Al-Rub, R.K. MSLattice: A Free Software for Generating Uniform and Graded Lattices Based on Triply Periodic Minimal Surfaces. *Mater. Des. Process. Commun.* **2023**, *3*, e205. [CrossRef]
39. Feng, J.; Fu, J.; Yao, X.; He, Y. Triply Periodic Minimal Surface (TPMS) Porous Structures: From Multi-Scale Design, Precise Additive Manufacturing to Multidisciplinary Applications. *Int. J. Extrem. Manuf.* **2022**, *4*, 022001. [CrossRef]
40. Kaur, I.; Singh, P. Flow and Thermal Transport Characteristics of Triply-Periodic Minimal Surface (TPMS)-Based Gyroid and Schwarz-P Cellular Materials. *Numer. Heat Transf. Part A Appl.* **2021**, *79*, 553–569. [CrossRef]
41. Baccoli, R.; Kumar, A.; Concas, A.; Gatto, G.; Pintus, N.; Medda, A.; Rodriguez, G. Thermal Diffusivity from Fourier's Inverse Problem Supervised by an Optimization Model: Theoretical Analysis and Experimental Validation. *Case Stud. Therm. Eng.* **2022**, *40*, 102533. [CrossRef]
42. Baccoli, R.; Sollai, F.; Medda, A.; Piccolo, A.; Fadda, P. An Adaptive Nonlinear Autoregressive ANN Model for High Time Resolution Traffic Noise Predictions. *Build. Environ.* **2022**, *207*, 108551. [CrossRef]
43. Majumder, A.; Achenza, M.; Mastino, C.C.; Baccoli, R.; Frattolillo, A. Thermo-Acoustic Building Insulation Materials Fabricated with Recycled Fibers—Jute, Wool and Loofah. *Energy Build.* **2023**, *293*, 113211. [CrossRef]

44. Kreith, F.; Manglik, R.M.; Bohn, M.S. *Principles of Heat Transfer*, 7th ed.; Cengage Learning: Stamford, CT, USA, 2010.
45. Lodi, M.B.; Bellizzi, G.; Paulis, A.; Grandi, N.; Palmeri, R.; Sekehravani, E.A.; Crocco, L.; Fanti, A.; Scapaticci, R. Electromagnetic Characterization and Biocompatibility Assessment of Magnetic Materials for Biomedical Applications. In Proceedings of the 2025 19th European Conference on Antennas and Propagation (EuCAP), Stockholm, Sweden, 30 March–4 April 2025.